



Marangoni Effect in Bipropellant Droplet Mixing during Hypergolic Ignition

Kai Sun (孙凯)^{1,*} Feifei Jia (贾飞飞)¹ Peng Zhang (张鹏)² Lingyun Shu (树凌云)¹ and Tianyou Wang (王天友)¹

¹State Key Laboratory of Engines, Tianjin University, Tianjin 300072, P.R. China

²Department of Mechanical Engineering, The Hong Kong Polytechnic University, Hung Hom, Hong Kong 999077, P.R. China



(Received 6 November 2020; revised 16 February 2021; accepted 22 February 2021; published 25 March 2021)

Hypergolic ignition of a bipropellant is an intrinsically nonpremixed physicochemical process that involves both chemistry and fluidic mixing. While the ignition delay time (IDT) of various hypergolic propellants has been extensively measured by using the prevalent droplet test, the effect of fluidic mixing on the hypergolic ignition process has rarely been studied. Compared with the well-understood droplet mixing within the same liquid, a prominent feature of bipropellant droplet mixing is the substantial surface tension difference, which induces a Marangoni effect upon droplet coalescence; however, it has not been addressed by previous hypergolic ignition studies and still remains inadequately understood. In this work, we numerically study the internal mixing of colliding droplets of different surface tensions with implications for hypergolic propellant ignition. The results show that the Marangoni effect substantially enhances droplet mixing compared with the situation without surface tension difference, and indicate the Marangoni effect could be a pivotal physical mechanism in hypergolic ignition. In particular, we identify an interesting phenomenon in that the Marangoni effect yields a nonmonotonic variation of internal mixing with increasing impact inertia, and this provides a likely interpretation of the nonmonotonic variation of the IDT experimentally observed by Zhang *et al.* [Combust. Flame 173, 276–287 (2016)]. Although binary droplet collision is employed as the specific object of the study, the present results could also provide insight into the hypergolic ignition of a bipropellant using various mixing methodologies, such as impinging jet and droplet-pool impact.

DOI: [10.1103/PhysRevApplied.15.034076](https://doi.org/10.1103/PhysRevApplied.15.034076)

I. INTRODUCTION

Hypergolic bipropellants are promising for high-performance propulsion systems such as rockets and missiles. In such systems, the fuel and the oxidizer are separately injected into the combustion chamber, and self-ignition is initiated by the liquid-phase chemical reactions in the merged mass. Since the engines do not need an extra ignition system but rely on the spontaneous ignition of the impinging liquid jets, they are less complex in design and more reliable in operation [1,2], and they have been attracting increasing interests in recent years.

In order to understand the hypergolic ignition of bipropellants, a few experimental methodologies have been developed, including the rapid-mixing reactor test [3–6], impinging jet test [7–10], and droplet impact test [11–30]. For the droplet impact test, a fuel or oxidizer droplet may impact onto an oxidizer or fuel interface of either a liquid pool [11–21], or a wall-deposited droplet [22–26], or

another droplet in ambient gas [27–30]. Using these experimental methodologies, the hypergolic ignition process of various bipropellants has been widely studied [3–30]. In these experimental works, attention has been paid to the propellant properties [7,11–19,22–25] and addition of catalysts [12,15,20–22], as well as ambient conditions [11,12,15], which primarily affect the hypergolic ignition process through chemistry.

It should be noted, however, that the hypergolic ignition of bipropellants is intrinsically nonpremixed and therefore not only involves chemistry but also largely depends on fluidic mixing. Although significant, the effect of fluidic mixing on the hypergolic ignition of bipropellants has rarely been studied. In this regard, we note that the impinging jet tests of Dennis *et al.* [8] and Bittner *et al.* [9] and the droplet-pool impact tests by Forness *et al.* [23] and Dambach *et al.* [25] showed that a higher impact inertia between the fuel and the oxidizer significantly enhances liquid-phase mixing and therefore shortens the ignition delay time (IDT). More recently, Zhang *et al.* [27–30] experimentally studied the hypergolic ignition of colliding propellant droplets. As illustrated in Fig. 1, their results

*sunkai@tju.edu.cn

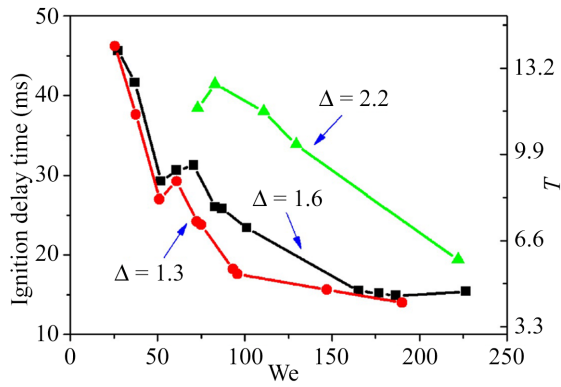


FIG. 1. Nonmonotonic variation of the ignition delay time (IDT) on the impact inertia (represented by the Weber number) for a N,N,N',N'-tetramethylethylenediamine (TMEDA) droplet colliding with a white fuming nitric acid (WFNA) droplet. Δ is the droplet size ratio. T is the IDT normalized by the droplet oscillation time $\sqrt{\rho_o R_o^3 / \sigma_o}$, where the subscript o denotes the oxidizer droplet. Reprinted from Zhang *et al.* [27] with permission of Elsevier.

further highlighted the pivotal role of fluidic mixing on the IDT, as the IDT tends to shorten substantially (by over a factor of 3) with increasing impact inertia (represented by the Weber number, We) as a result of enhanced fluidic mixing prior to ignition. A counter-intuitive phenomenon was also reported; the IDT conversely increases at an intermediate range of Weber number, which contradicts the traditional understanding that an increased momentum strengthens fluid motion and hence facilitates mixing [8,9,23,25]. Such nonmonotonicity fundamentally indicates complex physical mechanisms in bipropellant droplet mixing that significantly affect hypergolic ignition; however, this phenomenon has not been given due recognition by our combustion community.

Although fluidic mixing has rarely been considered in hypergolic ignition studies, one may question if the underlying physics has been addressed in fluid dynamics studies on droplet impact. In this regard, we note that a few works have been devoted to understanding the internal mixing of colliding droplets of the same surface tension [31–35]. For bipropellants, however, the fuel and the oxidizer are different liquids and their surface tensions could be considerably different. To quantify the difference, we summarize the bipropellants of previous experimental studies on hypergolic ignition in Table I. It is seen that the surface tensions of fuels are substantially lower when compared with those of the oxidizers, and for most cases the surface tension ratio between the fuel and the oxidizer, $\sigma_{\text{fuel}}/\sigma_{\text{oxidizer}}$, is in the range of 0.3–0.7. Therefore, the Marangoni effect could be non-negligible upon coalescence of the droplets; however, this has not been recognized in previous studies on hypergolic ignition studies. As extensively reviewed by Lohse and Zhang [36], the droplet coalescence process

substantially differs between situations with or without surface tension difference. In the presence of surface tension difference, the Marangoni effect yields encapsulation of the droplet of higher surface tension by the droplet of lower surface tension. For miscible liquids, Koldewij *et al.* [37] revealed a power law of $L(t) \sim t^{3/4}$, where $L(t)$ denotes the spreading distance of the lower surface tension fluid over the merged droplet surface, with t being time. Within the merged mass, Blanchette *et al.* [38] and Jia *et al.* [39] observed enhanced vortical mixing upon convergence of the Marangoni flow. The Marangoni-driven encapsulation of colliding droplets has been further employed as an in-air microfluidics platform for rapid fabrication of emulsions, suspensions, etc. [40].

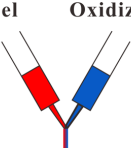
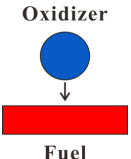
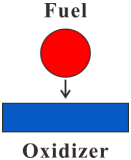
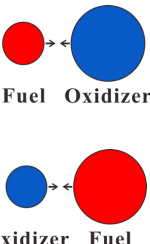
In spite of these worthy advances, however, the Marangoni effect on the hypergolic ignition process could be even more complicated and still remains inadequately understood. This is because the impinging jet in hypergolic propellant engines results in violent atomization, and hypergolic ignition largely occurs within colliding fuel-oxidizer droplets of various impact inertia and size disparities. Therefore, the surface tension gradient could either align with or oppose the droplet size gradient (the droplet size ratio determines the global equivalence ratio of the bipropellant), thereby forming different droplet impact scenarios with distinct fluid dynamic behaviors. In view of these considerations, this paper aims to numerically study the Marangoni effect on the internal mixing of colliding droplets and explore its potential influence on the IDT. Although binary droplet collision is employed as the specific problem in the present study, the results could also provide insight to understand the fluidic mixing in the hypergolic ignition process with various liquid-phase-mixing methods, such as impinging jet and droplet-pool impact. In the following, the numerical methods, results and discussion, and concluding remarks will be sequentially presented from Secs. II–IV.

II. NUMERICAL METHODS

A. Problem statement

Head-on binary droplet collision is employed as the specific type of droplet mixing, which can be regarded as a representative process in the hypergolic ignition of impinging jets in hypergolic propellant engines. From the fluid dynamic point of view, binary droplet collision shares similarities with impinging jet and droplet-pool impact processes. Specifically, the impinging jet can be viewed as two liquid columns impacting in cross section, and can be conceptually viewed as a two-dimensional droplet collision without a radial curvature; the droplet-pool impact can be regarded as a limiting case of binary droplet collision between droplets of unequal size, with the larger droplet size set to infinity.

TABLE I. A summary of bipropellants used in previous experimental studies on hypergolic ignition.

Test method	Schematic	Fuel	Oxidizer	$\sigma_{\text{Fuel}}/\sigma_{\text{Oxidizer}}$	Reference
Impinging jet		Furfuryl alcohol	WFNA	~ 1	McKinney <i>et al.</i> [3]
		Anhydrous hydrazine	HNO ₃	~ 0.7	Kilpatrick <i>et al.</i> [4]
		Triethylamine	WFNA	~ 0.6	Schalla <i>et al.</i> [5]
		MMH	RFNA	~ 0.4	Dennis <i>et al.</i> [8]
Droplet-pool impact		Triglyme	H ₂ O ₂ (90 wt%)	~ 0.4	Kang <i>et al.</i> [13]
		Tetraglyme	H ₂ O ₂ (90 wt%)	~ 0.4	Kang <i>et al.</i> [13]
		Propylamine	H ₂ O ₂ (90 wt%)	~ 0.3	Kang <i>et al.</i> [13]
		n-Butylamine	H ₂ O ₂ (90 wt%)	~ 0.3	Kang <i>et al.</i> [13]
		Pyridine	H ₂ O ₂ (90 wt%)	~ 0.4	Kang <i>et al.</i> [13]
		DETA	H ₂ O ₂ (90 wt%)	~ 0.5	Kang <i>et al.</i> [13]
		UDMH	WFNA	~ 0.7	Bhosale <i>et al.</i> [16]
		MMH	HNO ₃ (70 wt%)	~ 0.5	Wang <i>et al.</i> [18]
		MMH	HNO ₃ (90 wt%)	~ 0.4	Wang <i>et al.</i> [18]
		MMH	WFNA	~ 0.6	Forness <i>et al.</i> [23]
		BMIMDCA	RFNA	~ 0.5	Dambach <i>et al.</i> [19]
		DMAZ	RFNA	~ 0.3	Dambach <i>et al.</i> [19]
		TD	RFNA	~ 0.3	Dambach <i>et al.</i> [19]
		TMEDA	RFNA	~ 0.5	Dambach <i>et al.</i> [19]
		DMAZ	H ₂ O ₂ (98 wt%)	~ 0.3	Florczuk <i>et al.</i> [20]
		MEA	H ₂ O ₂ (98 wt%)	~ 0.5	Florczuk <i>et al.</i> [20]
		Methanol	H ₂ O ₂ (98 wt%)	~ 0.3	Florczuk <i>et al.</i> [20]
		Methanol	70% HNO ₃	~ 0.4	Forness <i>et al.</i> [23]
		MMH	RFNA	~ 0.4	Dambach <i>et al.</i> [19], Forness <i>et al.</i> [23], Dambach <i>et al.</i> [25]
					Zhang <i>et al.</i> [27–30]
Droplet-droplet impact		TMEDA	WFNA	~ 0.6	
		Ethanolamine solution of NaBH ₄	H ₂ O ₂ (92 wt%)	~ 0.6	Zhang <i>et al.</i> [29]

Abbreviations: BMIMDCA, 1-Butyl-3-Methylimidazolium Dicyanamide; DETA, Diethylenetriamine; DMAZ, 2-Azido-N,N-dimethylethanamine; MEA, Ethanolamine; MMH, Monomethyl hydrazine; RFNA, Red fuming nitric acid; TD, Solution of 34 wt% DMAZ and 66 wt% TMEDA; N,N,N',N'-Tetramethylethylenediamine; UDMH, Unsymmetrical dimethyl hydrazine; WFNA, White fuming nitric acid.

A full-physics-resolved modeling of the hypergolic ignition process is extremely complex and challenging because it involves a number of subprocesses of multiple time and/or spatial scales, including droplet dynamics, Marangoni flow, liquid-phase chemical reactions, heat transfer, vaporization, etc. To the authors' knowledge, such comprehensive modeling has never been attempted and is one of the most desired goals in future studies of this field. Therefore, in the present study, we neglect the chemical reactions and the associated heat release and heat transfer to separate the intrinsic Marangoni effect between the fuel

and oxidizer on the droplet mixing and discuss its possible influence on the ignition process.

We also note that surface tension is a strong function of temperature and heat release may also induce thermal Marangoni flows, but this is not included in the present simulations. According to Zhang *et al.* [27,29], the hypergolic ignition of colliding droplets can be divided into three stages: (1) droplet collision; (2) droplet heating and slow vaporization; (3) fast vaporization before ignition occurs. Stage 1 is an almost purely fluid dynamical process, accounting for 10%–15% of the IDT. Stage 2

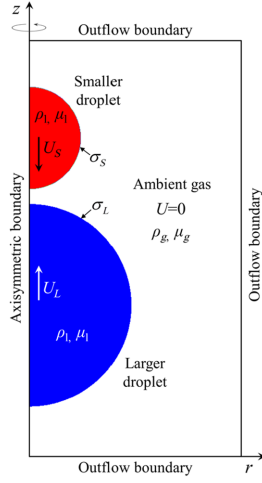


FIG. 2. Specifications of the computational domain and initial/boundary conditions.

accounts for about 50%–55%, and Stage 3 for 30%–40% of the IDT [27,29]. The droplet heating requires quite some time to increase the surface temperature (Stage 1 + Stage 2 account for 60%–70% of the IDT). Therefore, it is reasonable to assume a constant-temperature surface tension coefficient to understand the effect of fluidic mixing during the ignition process. In Sec. III, the possible thermal Marangoni effect due to heat release and uneven heat transfer will be discussed separately.

Head-on droplet collision is intrinsically symmetric with respect to the axis connecting the centers of mass of the two droplets, provided the impact inertia is not large enough to cause circumferential instabilities. As shown in Fig. 2, two droplets of diameter D_S and D_L (the subscripts S and L denote small and large, respectively) are placed in the initially stationary gaseous environment, with their velocities U_S and U_L set to make the total momentum of the system zero. The symmetric boundary condition is imposed on the axis, and the outflow boundary condition is applied on the other boundaries. For practical bipropellants, the fuel is typically miscible with the oxidizer to allow rapid and intimate mixing. Therefore, in our simulations, the two liquids are assumed to be fully miscible with only interfacial tension on the liquid-gas interface. The droplets are assumed to have identical liquid-phase density, ρ_l , and dynamic viscosity, μ_l , while their liquid-gas interfaces are given different surface tensions of σ_S and σ_L . Among σ_S and σ_L , we denote the smaller value to be σ_{sm} and the larger value to be σ_{lg} . The assumptions made in the simulations are summarized in Table II.

B. Governing equations

The two-phase flow is modeled using the phase-field method [41,42]. The composition C denotes the local fraction of liquid in the total fluid by volume, and its evolution

TABLE II. Assumptions in the simulations.

No.	Assumptions
1	two liquids are miscible
2	no chemical reaction, heat transfer, and phase change
3	two liquids have equal density of ρ_l
4	two liquids have equal viscosity of μ_l

is governed by the Cahn-Hilliard equation

$$\frac{\partial C}{\partial t} + \mathbf{u} \cdot \nabla C = M \nabla^2 \mu_C, \quad (1)$$

where \mathbf{u} is the fluid velocity, M is the interface mobility, and $\mu_C = \mu_0 - k \nabla^2 C = \partial E_0 / \partial C - k \nabla^2 C$ is the chemical potential, with E_0 being the bulk free energy and k the gradient factor. The bulk free energy takes the form of a double-well function, $E_0 = \beta C^2 (1 - C)^2$, and the chemical potential is given by $\mu_C = \beta (4C^3 - 6C^2 + 2C) - k \nabla^2 C$ [43,44]. For single-component two-phase flows, β and k are constants that determine the surface tension and the interface thickness by $\sigma = \sqrt{2k}/6$ and $\xi = \sqrt{8k}/\beta$, respectively.

In the present simulations, the liquid phase is composed of two miscible components and we have $C = C_1 + C_2$. Both two components should have their respective contribution to the Cahn-Hilliard diffusion, with the proportions being C_1/C and C_2/C , respectively. Therefore, the governing equation of C_1 takes the form

$$\frac{\partial C_1}{\partial t} + \mathbf{u} \cdot \nabla C_1 = \nabla \cdot (D \nabla C_1) + (C_1/C) M \nabla^2 \mu_C, \quad (2)$$

where the first term on the right-hand side (rhs) denotes molecular diffusion with D being the composition diffusivity, and the second term on the rhs describes the partial contribution of this composition to the total Cahn-Hilliard diffusion.

The nondimensional local surface tension σ/σ_L is determined by C_1/C , which usually shows a concave function for binary miscible fluid systems. In the present study, we model such a dependency by using a water/ethanol-solution system as $\sigma/\sigma_L = f[(C_1/C)f^{-1}(\sigma_S/\sigma_L)]$, in which f is a fitting function in the form of

$$f(x) = ae^{bx} + ce^{dx} + e, \quad (3)$$

where $a = 0.2155$, $b = -0.03727$, $c = 0.4952$, $d = -0.2996$, and $e = 0.2876$, and f^{-1} is its reverse function [45]. Although we use these specific numbers with four significant digits for line fitting, our quantitative results are not sensitive to them and the qualitative conclusions are even independent of the shape of the curve. This agrees

with the simulations of Blanchette [38] that show that the droplet coalescence process is primarily determined by the surface tension ratio and is rather insensitive to the specific dependence of surface tension on fluid composition.

The temporal and spatial variation of the surface tension of the liquid-gas interface is realized through k and β . To maintain a uniform interface thickness and a uniform rate of Cahn-Hilliard diffusion, we let $k = k_0\sigma/\sigma_L$, $\beta = \beta_0\sigma/\sigma_L$, and $M = M_0/(\sigma/\sigma_L)$, where k_0 , β_0 , and M_0 are constants.

Furthermore, the continuity equation and the momentum equation for incompressible flows are

$$\nabla \cdot \mathbf{u} = 0 \quad (4)$$

and

$$\rho \left(\frac{\partial \mathbf{u}}{\partial t} + \mathbf{u} \cdot \nabla \mathbf{u} \right) = -\nabla p + \nabla \cdot [\mu(\nabla \mathbf{u} + \nabla \mathbf{u}^T)] + \mu_C \nabla C + |\nabla C|^2 \nabla k - (\nabla k \times \nabla C) \nabla C, \quad (5)$$

where p is the pressure, and μ is the dynamic viscosity. On the rhs of Eq. (5), the third term represents surface tension and the fourth term is the Marangoni stress. The local fluid density and dynamic viscosity are taken to be linear functions of C by

$$\rho = \rho_l C + \rho_g(1 - C), \quad (6)$$

and

$$\mu = \mu_l C + \mu_g(1 - C). \quad (7)$$

C. Numerical implementation

Among the four governing Eqs. of (1), (2), (4), and (5), Eqs. (1), (4), and (5) are numerically solved using the lattice Boltzmann method (LBM), which has been developed to be an efficient flow solver in recent years [46–50]. In the LBM simulation, one distribution function is used to recover Eq. (1) and another distribution function is used to recover Eqs. (4) and (5) [43,44,50]. Detailed transformation from the governing equations to the LBM evolution equations in an axisymmetric coordinate can be

referred to in the authors' previous paper [50]. Equation (2) is not included in the framework LBM but is instead solved using the finite difference method with the third-order Runge-Kutta method [51] for time discretization and the fifth-order weighted essentially non-oscillatory scheme [52] for spatial discretization.

According to dimensional analysis, the flow similarity of the present problem can be described by seven nondimensional parameters: the Weber number, We ; the surface tension ratio, σ^* ; the droplet size ratio, Δ ; the Ohnesorge number, Oh ; the Schmidt number, Sc ; the liquid-gas density ratio, ρ^* ; and the liquid-gas viscosity ratio, μ^* , whose definitions are summarized in Table III. In the present simulations, ρ^* and μ^* are fixed at typical values for a liquid-gas system, at 500 and 50, respectively; therefore, the inertia and viscous effects from the ambient gas are negligible. The Oh number takes two values, 0.01 and 0.1. The mutual diffusion coefficient between the two liquids (D) is included in the Sc . For typical liquids, $\mu_l \sim O(10^{-3})$ Pa s, $\rho_l \sim O(10^3)$ kg/m³, and $D \sim O(10^{-9})$ m²/s; therefore, in the simulations Sc takes a typical value of 10^3 for a binary liquid system at the benchmark $Oh = 0.01$, and a larger value of 10^4 at $Oh = 0.1$ by using a fixed binary-fluid diffusivity; Δ is fixed at 2.0 and σ^* takes the two values of 0.5 and 2.0, which correspond to the two scenarios of (a) the Marangoni effect without a capillary pressure gradient between the droplets ($2\sigma_S/R_S = 2\sigma_L/R_L$ for $\sigma^* = 2$, where R denotes the droplet radius) and (b) the Marangoni effect combined with a capillary pressure gradient from the smaller droplet to the larger droplet ($2\sigma_S/R_S > 2\sigma_L/R_L$ for $\sigma^* = 0.5$). The Weber number varies in the range of 0–50, which is far below the threshold ($We_c \sim 150$) beyond which circumferential instabilities emerge and the axisymmetric assumption fails [53–55]. In the TMEDA/WFNA bipropellant system for instance, such a range of We corresponds to an impact velocity of approximately 0–4 m/s for a larger droplet size of 100 μ m, and an impact velocity of approximately 0–12 m/s for a larger droplet size of 10 μ m.

In phase-field modelling of two-phase flows, we also introduce an interface Péclet number (Pe_i) to measure the ratio between the convective and diffusive transports of the interface. According to Eq. (1), the diffusivity of the interface can be estimated by $D_{\text{interface}} = M_0\beta_0$ to measure the intensity of the Cahn-Hilliard diffusion. The

TABLE III. Nondimensional parameters in the simulations.

Nondimensional parameter	Definition	Value/Range
Weber number	$We = \rho_l D_L U^2 / \sigma_{lg}$	0–50
Surface tension ratio	$\sigma^* = \sigma_L / \sigma_S$	0.5, 1.0, 2.0
Droplet size ratio	$\Delta = D_L / D_S$	2.0
Ohnesorge number	$Oh = \mu_l / \sqrt{\rho D_L \sigma_{lg}}$	0.01, 0.1
Schmidt number	$Sc = \mu_l / (\rho_l D)$	10^3 (at $Oh = 0.01$), 10^4 (at $Oh = 0.01$)
Liquid-gas density ratio	$\rho^* = \rho_l / \rho_g$	500
Liquid-gas viscosity ratio	$\mu^* = \mu_l / \mu_g$	50

characteristic velocity of the interface due to capillarity can be estimated by $U_{\text{interface}} \sim \sqrt{\sigma_L/(\rho_l R_S)}$. Therefore, Pe_i can be given by $\text{Pe}_i = U_{\text{interface}} \xi / D_{\text{interface}} = \xi \sqrt{[\sigma_L/(\rho_l R_S)]} / (M_0 \beta_0)$, which is fixed at 1.34 in the present simulations to keep the liquid-gas interface close to the equilibrium profile throughout the droplet collision process. Time is normalized as $t^* = (t - t_0)/t_{\text{osc}}$, where t_0 denotes the onset of droplet contact, and $t_{\text{osc}} = \sqrt{\rho R_L^3 / \sigma_{lg}}$ is the characteristic droplet oscillation time.

The numerical method has been validated against experiments on the coalescence/impact of a water droplet on an ethanol pool in the authors' previous works [34,39]. In the present study, we further validate our code by successfully reproducing the theoretical scaling law of $L(t) \sim t^{3/4}$ for the spreading distance of the lower-surface-tension fluid upon droplet coalescence (see Fig. S1 of the Supplemental Material [56] for numerical validation of the temporal evolution of the spreading distance of the lower-surface-tension fluid). We also successfully reproduce the numerical results of Blanchette [38] on the internal mixing of two initially stationary droplets of different surface tensions. Regarding the grid resolution of the present simulations, $D_S/\xi = 60$ shows insignificant grid dependency at an acceptable computational cost (see Figs. S2 and S3 of the Supplemental Material [56] for the grid dependency study), and this is therefore employed to produce the following results.

D. Quantification of internal mixing

To quantify the degree of internal mixing, a mixing parameter $\phi(\mathbf{x}, t)$ is defined at each grid location \mathbf{x} inside the droplet at time t as

$$\phi(\mathbf{x}, t) = C_1(\mathbf{x}, t)/C(\mathbf{x}, t). \quad (8)$$

Therefore, the pure lower-surface-tension fluid and the pure higher-surface-tension fluid can be distinguished by $\phi = 1$ and $\phi = 0$, respectively. Considering that mixing occurs with $0 < \phi < 1$ and maximizes at $\phi = 0.5$, we define a temporal-varying global mixing index $\Phi(t)$ of the merged droplet as

$$\Phi(t) = 1 - \sqrt{\frac{\int (2\phi(\mathbf{x}, t) - 1)^2 dV}{V}}, \quad (9)$$

in which V denotes the volume of the droplet, and the second term on the right-hand side is the covariance of ϕ over the entire volume of the droplet.

Furthermore, as heat is released and accumulated prior to ignition for hypergolic droplets, we also define a

cumulative mixing index as [32]

$$\Phi_c(T) = \int_0^T \Phi(t) dt. \quad (10)$$

From Fig. 1, the normalized IDT that shows nonmonotonic variation with the Weber number is around $t^* = 8$. Therefore, in the present study, we are particularly interested in comparing $\Phi(t)$ and $\Phi_c(T)$ at $t^* = 8$ to explore the possible influence of fluidic mixing on the variation of IDT. Such a timescale can provide us with information about the long-time droplet dynamics and internal mixing.

III. RESULTS AND DISCUSSION

A. Mixing of colliding droplets without surface tension difference

Before exploring the Marangoni effect on the mixing of colliding droplets, we first simulate a series of benchmark cases without surface tension difference ($\sigma^* = 1$) and plot the results in Fig. 3. Specifically, at $\text{We} = 0$, the convergence of capillary waves on the smaller droplet interface forms a protruding shape at $t^* = 0.5$, which then retracts and penetrates deep into the larger droplet under capillary pressure. If We is increased to 10, such a protruding shape cannot form due to the radially outward spreading motion, which yields a “domelike” mixing pattern with a reduced penetration depth. With further increasing We , the penetration depth of the smaller droplet increases again due to the enlarged axial driving force of impact inertia. Such results physically correspond to the nonmonotonic emergence of jetlike mixing in the merging of two droplets of unequal sizes, which was observed for water droplet collision by Tang *et al.* [31]. The reemerged internal jet structure at a

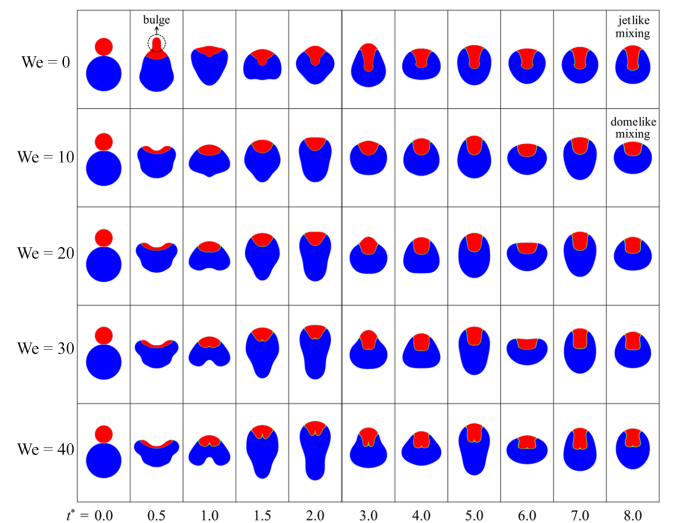


FIG. 3. Collision and mixing of droplets of the same liquid at different We and fixed $\sigma^* = 1$ and $\text{Oh} = 0.01$.

large We is less obvious in the present simulations compared with the water droplet collision experiment, since we use a higher Oh number and the viscous dissipation is more significant.

Quantitative comparisons of both the mixing index Φ and the cumulative mixing index Φ_c at different Weber numbers are shown in Fig. 4. From Fig. 4(a), the mixing index Φ increases monotonically with We during the very early stage ($t^* < 0.5$), since the radial spreading of the smaller droplet on the impact crater significantly enlarges the contact area of the two liquids and therefore facilitates mixing. Subsequently, however, mixing is governed by the axial penetration motion and the formation of the internal jet largely increases the mixing index. We also note that the mixing index increases with time due to continuous diffusion. Therefore, as illustrated in Figs. 4(a) and 4(b), both Φ and Φ_c at $t^* = 8$ present a nonmonotonic variation of “decrease-increase” with increasing We . Such a nonmonotonicity occurs for $We < 10$ and is caused by the aforementioned nonmonotonic emergence of the internal jet (see Figs. S4 and S5 of the Supplemental Material [56] for more refined results on the comparison of the mixing index and the cumulative mixing index at low Weber numbers).

B. Marangoni-driven mixing for colliding droplets of different surface tensions

By introducing a surface tension difference between the two droplets, the internal mixing of the merged droplet changes dramatically. Regardless of the exact mixing pattern, we first compare Φ_c for $\sigma^* = 0.5, 1.0$, and 2.0 at two distinct Weber numbers of 0 and 50. As shown in Fig. 5, the mixing enhancement caused by introducing a surface tension difference (compare the lines of different color but the same type) is more effective compared with the mixing enhancement caused by increasing the impact inertia (compare the solid lines with the dashed lines of same color). Furthermore, comparing $\sigma^* > 1$ and $\sigma^* < 1$, the former scenario yields even more enhanced mixing compared with

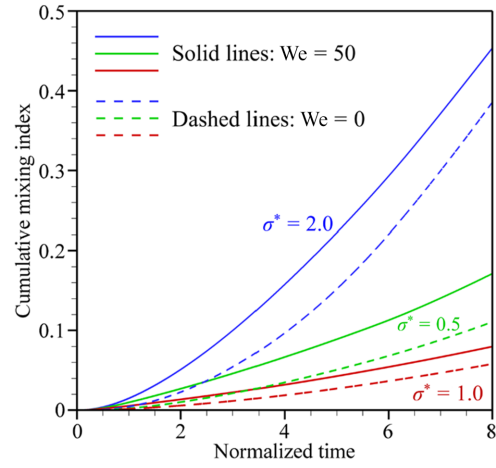


FIG. 5. Temporal evolution of the cumulative mixing index at different We and σ^* and fixed $Oh = 0.01$.

the latter, i.e., a smaller droplet of lower surface tension colliding with a larger droplet of higher surface tension is preferred for enhanced mixing. In the following, these two scenarios will be discussed separately.

1. Mixing of a smaller droplet of lower surface tension with a larger droplet of higher surface tension ($\sigma^* > 1$)

We first consider the scenario of $\sigma^* > 1$, i.e., a smaller droplet of lower surface tension colliding with a larger droplet of higher surface tension. Such a scenario corresponds to the stoichiometric condition of the TMEDA/WFNA bipropellant system and is physically similar to a lower-surface-tension fuel/oxidizer droplet dripping onto a higher-surface-tension oxidizer/fuel pool.

Figure 6(a) shows the droplet collision process at various Weber numbers and fixed $\Delta = 2$ and $\sigma^* = 2$. It is seen that, without capillary pressure difference between the two unequal-sized droplets ($2\sigma_L/R_L = 2\sigma_S/R_S$), the aforementioned capillary-pressure-driven jetlike mixing is no longer presented. Instead, the Marangoni effect governs the mixing process, i.e., the smaller droplet tends

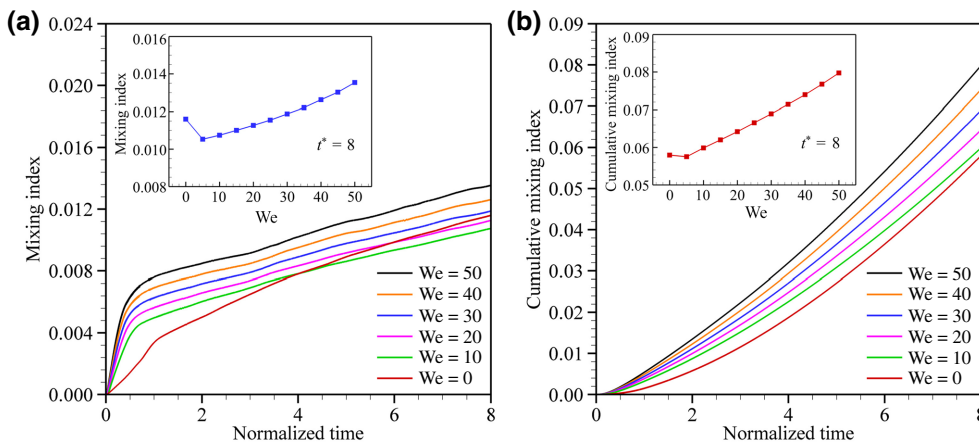


FIG. 4. Quantitative comparison of the internal mixing of the same liquid at different We and fixed $\sigma^* = 1$ and $Oh = 0.01$: (a) temporal evolution of the mixing index; (b) temporal evolution of the cumulative mixing index. The embedded insets compare the values at $t^* = 8$.

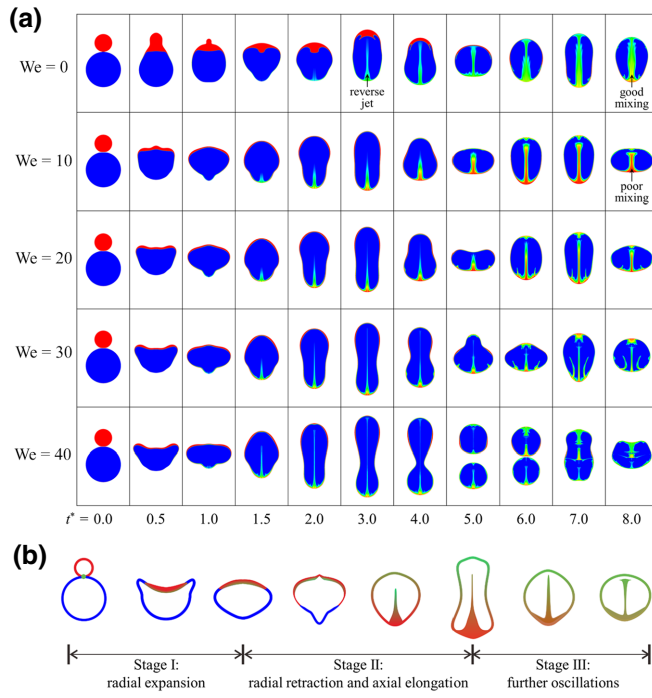


FIG. 6. (a) Collision and mixing of droplets at different We and fixed $\sigma^* = 2.0$ and $Oh = 0.01$. (b) Schematic of the three stages of the droplet collision process.

to wrap up the large droplet, and an inverse internal jet forms upon the convergence of the Marangoni flow at the far side of the larger droplet. At different Weber numbers, the inverse internal jet exhibits “good mixing” and “poor mixing”, which will be explained in the following. To visualize the Marangoni flow, we compare the flow fields of two cases with $We = 10$ shown in Figs. 6(a) and 3 in Fig. 7. Marangoni flow is clearly observed with a surface tension difference ($\sigma^* = 2.0$), as tangential flow is seen on the liquid-air interface and vortical recirculation is induced beneath the interface. For the other case without a surface tension difference ($\sigma^* = 1$), however, the flow field is distinct with vortical structures induced by interfacial oscillation only. For droplet collision with a surface tension difference, the interfacial Marangoni flow continuously entrains fluid of the larger droplet into the shear layer beneath the interface, thereby leading to a significant enhancement of mixing. For simplicity, we divide the droplet collision process into three stages as illustrated in Fig. 6(b): Stage I, the merged droplet expands radially (e.g., $t^* < 1$ for $We = 10$); Stage II, the droplet retracts radially and elongates axially (e.g., $1 < t^* < 3$ for $We = 10$); Stage III, the droplet retracts axially and further oscillates (e.g., $t^* > 3$ for $We = 10$).

A quantitative comparison of the internal mixing is shown in Fig. 8. As with the aforementioned benchmark cases of $\sigma^* = 1$, the mixing index increases with We during Stages I and II, while the Marangoni-driven mixing

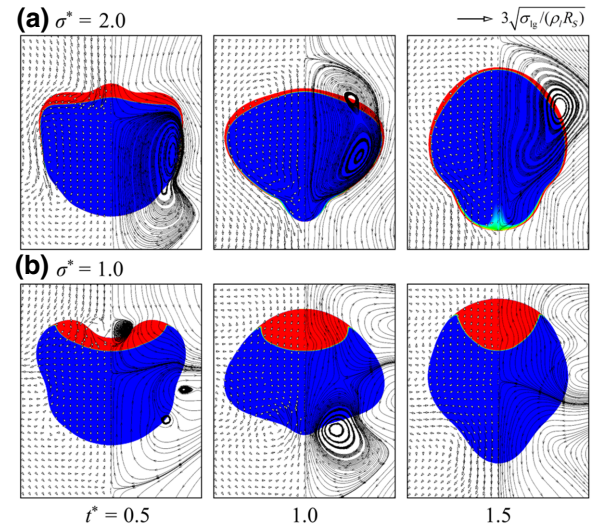


FIG. 7. Comparison of the flow fields of two cases in (a) Fig. 6 (a) with $\sigma^* = 2.0$; (b) Fig. 3 with $\sigma^* = 1$. The two cases have identical $We = 10$ and $Oh = 0.01$.

yields distinct behavior during Stage III. Both Φ and Φ_c at $t^* = 8$ present a nonmonotonic variation of decrease-increase-decrease-increase with We (see the figure insets). In this nonmonotonic variation, the increase of internal mixing with We is due to the enhanced impact-inertia-driven spreading motion, and we explain only the emergence of the two unexpected decreases of internal mixing with We in the following.

The first decrease of both Φ and Φ_c occurs in the We range of 0–10. At $We = 0$, as illustrated in Fig. 6(a), the retraction of the smaller droplet towards the larger droplet does not result in wide spreading on the surface at $t^* = 1$, and the accumulated smaller droplet liquid can only wrap up the larger droplet gradually by the interfacial Marangoni flow. As a result, the entrainment of the larger droplet liquid by the smaller droplet liquid during the “wrap up” process is substantial and the reverse internal jet is therefore composed of well-mixed fluids (colored in green), which finally yields a large mixing index at $t^* = 8$. When the Weber number is increased to 10, as illustrated in Fig. 6(a), the smaller droplet spreads more widely over the larger droplet surface, and the smaller droplet liquid constitutes a larger thickness of the Marangoni shear layer. Since mixing occurs in the vicinity of the surface of contact, while such a spreading motion results in a reduced contact-surface-area:smaller-droplet-volume ratio during the wrap up process (see Fig. 9), the outer smaller droplet fluid cannot readily mix with the larger droplet liquid but is transported into the droplet interior, and this process leads to a reverse internal jet of richer smaller droplet liquid and finally a decrease in the mixing index.

The second decrease of both Φ and Φ_c occurs for $30 < We < 40$. To explain this, we note that the displacement velocity of the lower-surface-tension liquid on the

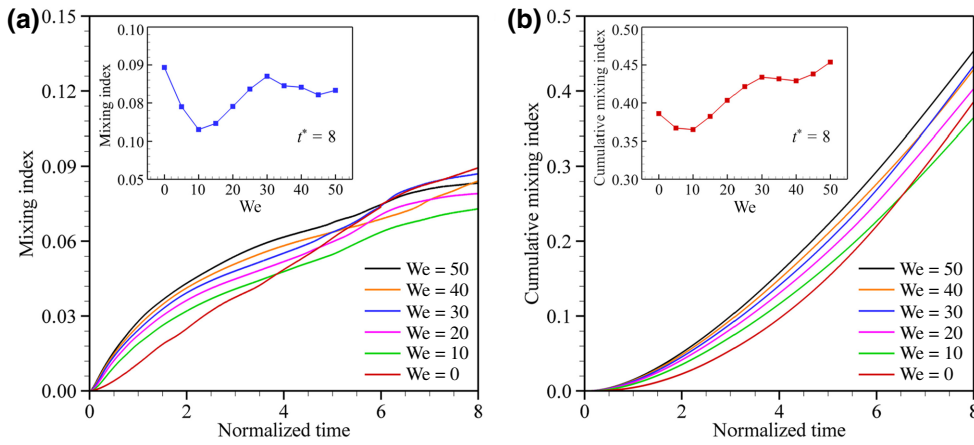


FIG. 8. Quantitative comparison of the internal mixing at different We and fixed $\sigma^* = 2.0$ and $Oh = 0.01$: (a) temporal evolution of the mixing index; (b) temporal evolution of the cumulative mixing index. The embedded insets compare the values at $t^* = 8$.

deforming interface, u_{dis} , is largely affected by the droplet deformation. As shown in Fig. 9, on the deformable interface u_{dis} can be decomposed into $u_{dis} = u_{MF} - u_{str}$, in which u_{MF} is the Marangoni flow velocity, and $u_{str} = dl_i/dt$ denotes the stretching velocity of the interface with l_i denoting the characteristic length of the deformed interface. With the increase of We , the increasing stretch effect causes (a) u_{str} to increase, and (b) the mixing front of the Marangoni flow to thicken and thereby reduce u_{MF} . Under these two effects, the impact-inertia-driven interface deformation increasingly counteracts the Marangoni flow, which is therefore unfavorable for Marangoni-driven mixing. As a result, although impact inertia facilitates early-stage mixing, it suppresses Marangoni-driven mixing during a later stage, and both Φ and Φ_c show decrease-increase at a high Weber number.

2. Mixing of a smaller droplet of higher surface tension with a larger droplet of lower surface tension ($\sigma^* < 1$)

Now we consider the opposite scenario of $\sigma^* < 1$, which corresponds to the stoichiometric condition of an

ethanolamine solution of $NaBH_4/H_2O_2$ bipropellant system and is physically similar to a higher-surface-tension fuel/oxidizer droplet dripping onto a lower-surface-tension oxidizer/fuel pool. In such a situation, the capillary pressure difference between the droplets $\Delta p = 2(\sigma_S/R_S - \sigma_L/R_L) = 2(1 - \sigma^*/\Delta)\sigma_S/R_S$ is not offset but is increased by the surface tension difference. Therefore, the surface tension difference imposes a combined Marangoni effect and enlarged capillary pressure difference to the droplet collision process compared with the benchmark cases of $\sigma^* = 1$.

As shown in Fig. 10(a), under these two synergistic effects, the smaller droplet penetrates the larger droplet more easily and yields rapid encapsulation. Although the capillary pressure difference is present and even enhanced, the capillary-driven jetlike mixing for $\sigma^* = 1$ is still not observed. This is caused by the Marangoni flow, which firstly detaches the smaller droplet fluid from the surface during the wrap up motion, and then transports it into the interior by the Marangoni-flow-induced internal circulating flow.

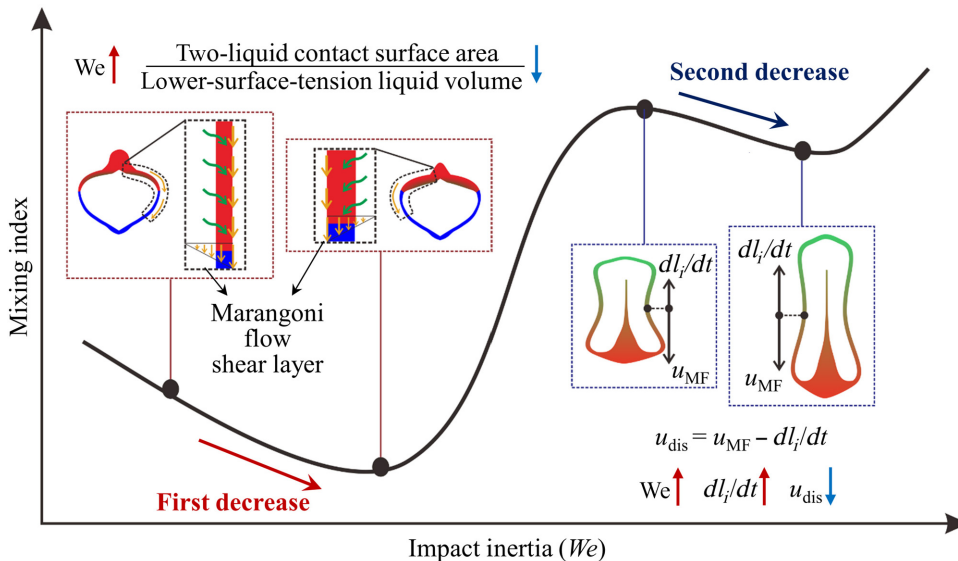


FIG. 9. Schematic of the non-monotonic variation of the mixing index with increasing We for $\sigma^* > 1$. In the figure, dl_i/dt denotes the stretching velocity of the interface, u_{dis} denotes the displacement velocity of the lower-surface-tension liquid, and u_{MF} denotes the Marangoni flow velocity.

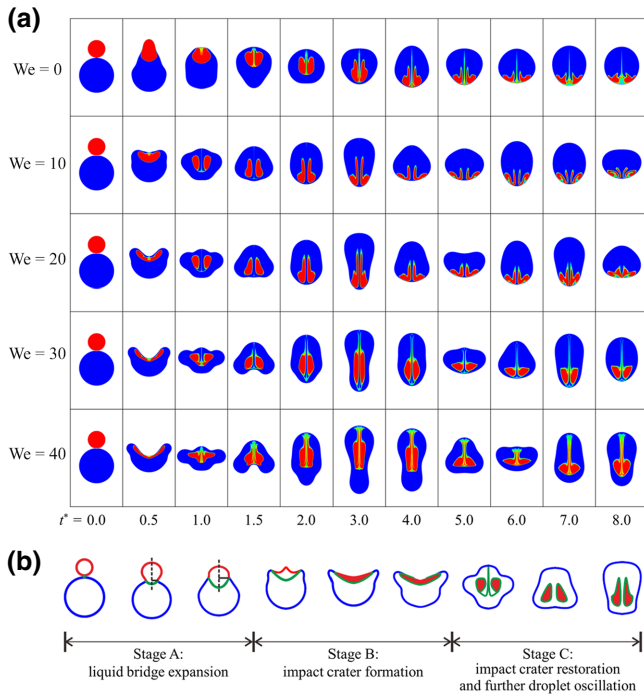


FIG. 10. (a) Collision and mixing of droplets at different We and fixed $\sigma^* = 0.5$ and $Oh = 0.01$. (b) Schematic of the three stages of the droplet collision process.

Quantitative comparison of the mixing indices at different We is shown in Fig. 11. With an increase in We , both Φ and Φ_c exhibit a nonmonotonic variation of increase-decrease-increase at $t^* = 8$. For simplicity, we divide the droplet collision process into three stages, as illustrated in Fig. 10(b): Stage A, a liquid bridge forms upon coalescence and expands radially, while the upper interface of the droplet is almost unaffected; Stage B, the radius of the liquid bridge reaches R_S and the impact crater is formed with the smaller droplet spreading on the crater surface; Stage C, the impact crater restores and the merged droplet further oscillates while the smaller droplet liquid detaches from the interface and is transported into the droplet interior. It

is noted that, these three stages A–C correlate with and differ from the aforementioned three stages I–III for $\sigma^* > 1$, as Stages A and B correspond to Stage I, and Stage C corresponds to Stages II and III. We use different definitions for these two scenarios since they have different timescales for the encapsulation of the higher surface tension droplet, which are of the order of $O(10)$ for $\sigma^* = 2.0$ and $O(1)$ for $\sigma^* = 0.5$ in the normalized time unit t^* . Therefore, the distinction between Stages A and B is insignificant for $\sigma^* = 2.0$, and the distinction between Stages II and III is neglected for $\sigma^* = 0.5$.

Similar to the previous discussions for $\sigma^* > 1$, the general increase of the mixing index with We for $\sigma^* < 1$ is also caused by the impact-inertia-driven spreading of the smaller droplet on the larger droplet surface during Stages A and B. This can be substantiated by Fig. 11(a), as the mixing index increases monotonically with We at $t^* < 1$. Therefore, the decrease of the mixing index at an intermediate range of We should also be caused by a negative influence of the impact inertia on the Marangoni-driven mixing.

With the increase in We , as shown in Fig. 12, during Stage A the radial expansion of the liquid bridge is accelerated by the impact inertia, which results in a shortened path for the Marangoni flow (denoted as l) and therefore facilitates encapsulation of the smaller droplet; during Stage B the radially inward Marangoni flow on the impact crater surface is weakened by the expanding velocity of the crater surface dl_{ci}/dt , where l_{ci} is the profile length of the crater surface. Therefore, the effect of impact inertia on the Marangoni-driven mixing is positive during Stage A and negative during Stage B, with the latter negative effect becoming increasingly prominent compared with the former positive effect with increasing We . As a result, the Marangoni-driven mixing is suppressed by the impact inertia beyond a certain Weber number, and the suppressed Marangoni-driven mixing could further counteract the enhanced impact-inertia-driven mixing at an intermediate range of We , thereby yielding the nonmonotonic

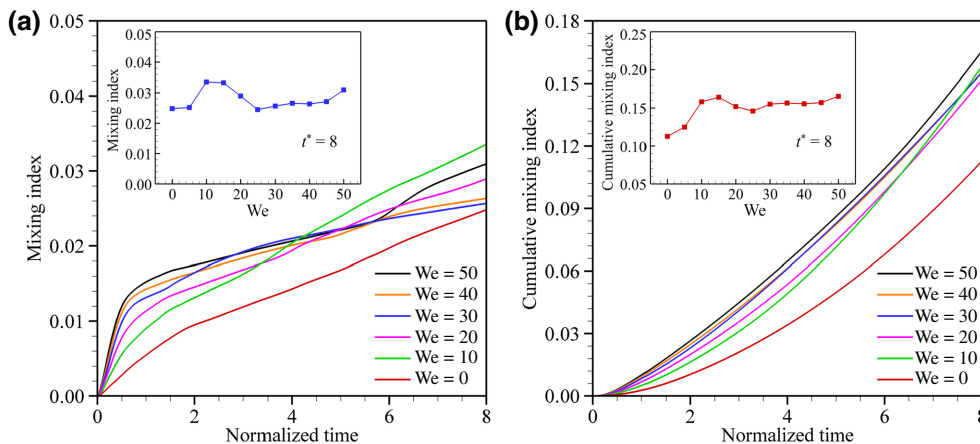


FIG. 11. Quantitative comparison of the internal mixing at different We and fixed $\sigma^* = 0.5$ and $Oh = 0.01$: (a) temporal evolution of the mixing index; (b) temporal evolution of the cumulative mixing index. The embedded insets compare the values at $t^* = 8$.

variation of the mixing index of increase-decrease-increase described previously.

Such increase-decrease-increase for $\sigma^* < 1$ fundamentally corresponds to the latter part of the decrease-increase-decrease-increase for $\sigma^* > 1$. The absence of the first decrease at a small Weber number for $\sigma^* < 1$ is rooted in the wrap up process. For $\sigma^* > 1$, the smaller droplet wraps up the larger droplet slowly, and substantial smaller droplet liquid is engaged in the Marangoni-driven mixing during the wrap up process. As mentioned in Sec. III, a slight impact inertia causes the smaller droplet to spread on the surface of the larger droplet rather than displace the entire large droplet surface, and the Marangoni-driven mixing per unit mass of the smaller droplet liquid is reduced. For $\sigma^* < 1$, in contrast, the smaller droplet penetrates into the larger droplet shortly after coalescence and only a small proportion of the smaller droplet liquid is involved in the Marangoni-driven mixing during the wrap up process. Therefore, the internal mixing largely relies on the long-time, post-wrap-up internal circulating flow rather than the short-time Marangoni-driven mixing during the wrap up process, and a slight impact inertia results in faster encapsulation and an increase in the mixing index.

C. Interpretation of the variation of IDT with impact inertia in hypergolic ignition experiments

So far, we have identified and explained the Marangoni-effect-induced nonmonotonic variations of internal mixing with increasing impact inertia. Now we further discuss its possible influence on the hypergolic ignition of bipropellants by interpreting the experimental results of Zhang *et al.* [27,29]. In their experiments, two types of bipropellant were used, namely TMEDA/WFNA and an ethanolamine

solution of NaBH_4 /hydrogen peroxide (H_2O_2), which will be discussed separately in the following.

1. Nonmonotonic decrease-increase-decrease of IDT with impact inertia for TMEDA/WFNA bipropellant

We first consider the stoichiometric condition of TMEDA/WFNA. In such a situation, the WFNA oxidizer droplet has a larger size and a higher surface tension and the TMEDA fuel droplet has a smaller size and a lower surface tension; this fundamentally corresponds to the scenario of $\sigma^* > 1$ discussed previously. As shown in Fig. 1, the IDT of the colliding bipropellant droplets shows a nonmonotonic variation of decrease-increase-decrease with the impact inertia, which could possibly correspond to a nonmonotonic variation of internal mixing of increase-decrease-increase. In this regard, we further note that the nonmonotonic variation of IDT with Weber number in the experiment of Zhang *et al.* [27] occurs for $50 < \text{We} < 60$ at $\Delta = 1.3$, $50 < \text{We} < 70$ at $\Delta = 1.6$, and $70 < \text{We} < 80$ at $\Delta = 2.2$. Therefore, it is reasonable to expect that the range of We at $\Delta = 2$ should be within 50–80. However, since the density of TMEDA (1500 kg/m^3) is only half the density of WFNA (780 kg/m^3), and We is defined based on the higher liquid density, the effective Weber number determined by neglecting such liquid density disparity should be substantially lower.

To estimate this effect, we note that the kinetic energy (KE) involved in the droplet collision process is $E_k = E_{k0} - E_{kf}$, in which E_{k0} denotes the initial kinetic energy of the two impacting droplets, and E_{kf} denotes the translational kinetic energy of the merged droplet. When $E_{kf} = 0$, i.e., the velocity of the center of mass of the merged droplet is zero, we have $E_k = E_{k0}$. Such a condition can be only achieved when the momentum of the colliding system is zero, which requires $\rho_S(4\pi R_S^3/3)U_S = \rho_L(4\pi R_L^3/3)U_L$

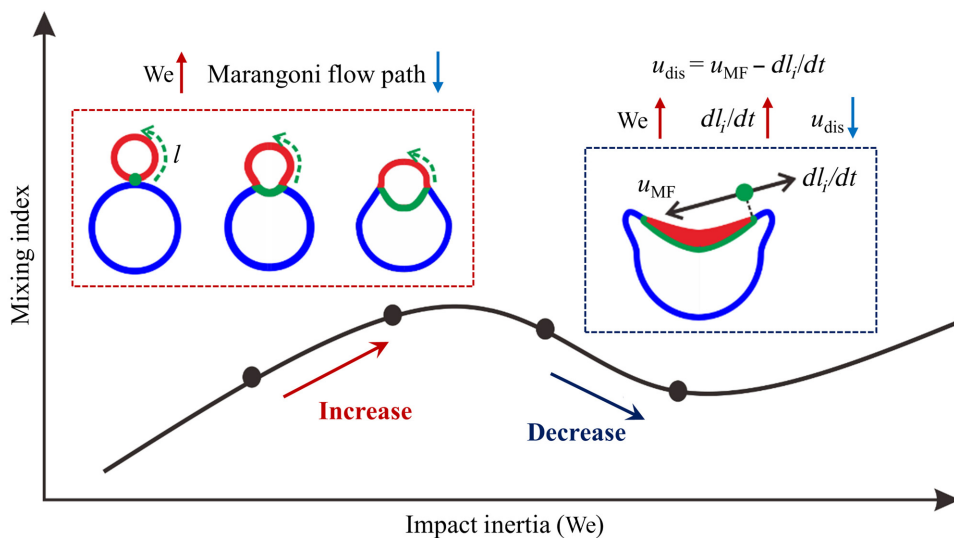


FIG. 12. Schematic of the nonmonotonic variation of the mixing index with increasing We for $\sigma^* < 1$. In the figure, l denotes the length of the Marangoni flow path, dl_i/dt denotes the stretching velocity of the interface, u_{dis} denotes the displacement velocity of the lower-surface-tension liquid, and u_{MF} denotes the Marangoni flow velocity.

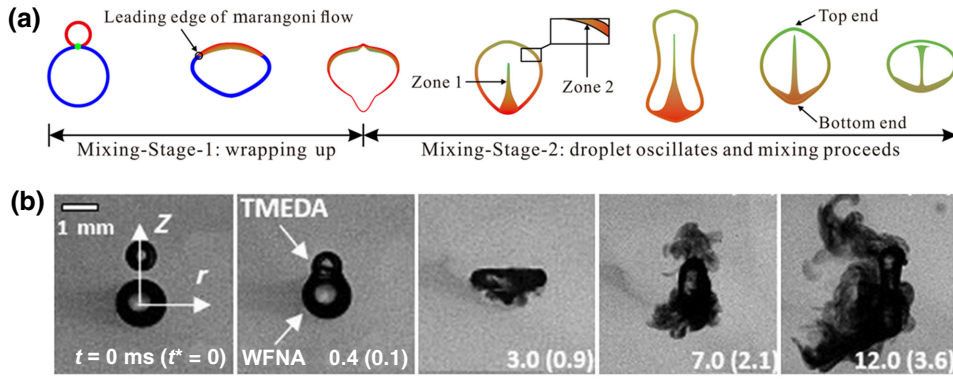


FIG. 13. (a) Schematic of the two stages of the droplet mixing process. Zone 1 denotes the mixing region of the reverse internal jet inside the droplet, and Zone 2 denotes the mixing region of the Marangoni shear layer beneath the droplet interface. (b) High-speed images for hypergolic ignition of colliding TMEDA/WFNA droplets ($We = 60.9$, $\Delta = 1.6$). Reprinted from Zhang *et al.* [27] with permission of Elsevier.

and equivalently $U_S/U_L = \Delta^3(\rho_L/\rho_S)$. Since the impact velocity is $U = U_S + U_L$, we further have

$$U_S = U \frac{\Delta^3(\rho_L/\rho_S)}{1 + \Delta^3(\rho_L/\rho_S)}, \quad (11)$$

and

$$U_L = U \frac{1}{1 + \Delta^3(\rho_L/\rho_S)}. \quad (12)$$

For $\Delta = 2$ and $\rho_L/\rho_S = 1$, we have $U_S = 8U/9$ and $U_L = U/9$, therefore

$$E_k = E_{k0} = \frac{1}{2} \rho_S (4\pi R_S^3/3) (8U/9)^2 + \frac{1}{2} \rho_L (4\pi R_L^3/3) (U/9)^2 = \frac{6\pi}{81} \rho_L R_L^3 U^2. \quad (13)$$

For $\Delta = 2$ and $\rho_L/\rho_S = 2$, we have $U_S = 16U/17$ and $U_L = U/17$, therefore

$$E_k = E_{k0} = \frac{1}{2} \rho_S (4\pi R_S^3/3) (16U/17)^2 + \frac{1}{2} \rho_L (4\pi R_L^3/3) (U/17)^2 = \frac{34\pi}{867} \rho_L R_L^3 U^2. \quad (14)$$

As such, at $\Delta = 2$ and a fixed ρ_L , the effective impact kinetic energy for $\rho_L/\rho_S = 2$ is only 52.9% compared with $\rho_L/\rho_S = 1$, indicating the effective Weber number for the nonmonotonic IDT should be within the range of 25–40. This agrees well with the aforementioned second decrease of the mixing index for $30 < We < 40$ in the present simulations. Therefore, since we have shown in Sec. III that capillary-induced jetlike mixing is absent for colliding droplets of unlike surface tensions and replaced by Marangoni-driven mixing, the nonmonotonic decrease-increase-decrease of IDT with increasing We for TMEDA/WFNA droplet collision should be fundamentally caused by the increase-decrease-increase of internal mixing. The unexpected increase of IDT at an intermediate Weber number is due to the negative effect

of impact inertia on the Marangoni-driven mixing, i.e., the increasing stretch of the deformed interface at high impact inertia weakens the Marangoni flow and thereby leads to decelerated internal mixing.

It should be also noted that the uneven heat release during the ignition delay may induce additional thermal Marangoni flow, since surface tension is a strong function of temperature. To address this issue, since the temperature equation is not solved in the present simulations, we further estimate the possible effects based on some scaling arguments. For clarity, we redivide the droplet mixing process into two substages as shown in Fig. 13(a): Mixing-Stage-1, in which the lower-surface-tension droplet fluid entirely wraps up the other droplet of higher surface tension; and Mixing-Stage-2, in which the merged droplet further oscillates and mixing proceeds until it self-ignites.

During Mixing-Stage-1, the spreading distance of the lower-surface-tension liquid over the higher-surface-tension droplet surface, $L(t)$, obeys a power law of $L(t) \sim [(\Delta\sigma)^2/(\rho_1\mu_1)]^{1/4} t^{3/4}$ [37,45]. Therefore, by letting $L(t) = \pi R_L$, the characteristic time of Mixing-Stage-1 can be estimated by $t_1 \sim [(\pi R_L)^4 \rho_1 \mu_1 / (\Delta\sigma)^2]^{1/3}$, which in normalized time units is $t_1^* = t_1/t_{\text{osc}} \sim \pi^{4/3} \text{Oh}^{1/3} / (1 - \sigma_{\text{sm}}/\sigma_{\text{lg}})^{2/3}$. For typical bipropellant systems with $(1 - \sigma_{\text{sm}}/\sigma_{\text{lg}}) \sim 0.5$ and $\text{Oh} = \mu_1/\sqrt{\rho_1 \sigma_{\text{lg}} D_L} \sim 0.01$, t_1^* is close to unity. Therefore, since the IDT generally takes several or tens of time units [27], Mixing-Stage-1 is rather short during the ignition process and can be assumed to be a pure fluid mechanical process without obvious exothermic reactions and temperature rise.

During Mixing-Stage-2, heat is continuously released and the droplet is being heated up. As shown in Fig. 13(a), there are two mixing regions that may react and release heat: (a) Zone 1, the mixing region of the converged reverse internal jet inside the droplet; (b) Zone 2, the mixing region of the Marangoni shear layer beneath the droplet interface. The normalized characteristic time for the heat transfer from the reacting zone to the droplet surface can be estimated by $t_{\text{thermal}}^* \sim (L_{\text{thermal}}^2/k_{\text{thermal}})/t_{\text{osc}}$, in which L_{thermal} denotes the characteristic length from the reacting zone to the droplet surface, and k_{thermal} is the

thermal diffusivity. For Zone 1, $L_{\text{thermal}} \sim R_L$ and therefore $t_{\text{thermal}}^* \sim \sqrt{(\sigma_{\text{lg}} R_L / \rho_l) / k_{\text{thermal}}} \sim O(10^2 - 10^3)$, indicating that the released heat cannot transfer to the droplet surface prior to ignition. For Zone 2, $L_{\text{thermal}} \sim \delta \sim R_L \sqrt{\text{Oh}}$ and we have $t_{\text{thermal}}^* \sim \text{Oh} \sqrt{(\sigma_{\text{lg}} R_L / \rho_l) / k_{\text{thermal}}} \sim (\mu_l / \rho_l) / k_{\text{thermal}} = \text{Pr}$, where Pr denotes the Prandtl number. For typical liquids, Pr is of the order of $O(1 - 10)$ and t_{thermal}^* is therefore comparable with the IDT, indicating the released heat in Zone 2 could be readily transferred to the droplet surface during Mixing-Stage-2.

According to our simulations, mixing at the leading edge of the Marangoni flow is more efficient since the shear flow continuously entrains the inner fluid. This indicates that during Mixing-Stage-2 an initial temperature gradient may establish on the droplet surface, with the bottom being at a higher temperature than the top, which could further induce thermal Marangoni flow from the bottom to the top. On the other hand, since the lower-surface-tension liquid tends to spread on the merged droplet surface with a relatively uniform thickness, the entire droplet surface could be gradually heated up. Therefore, the temperature gradient along the liquid-gas interface is expected to be insignificant, and the thermal-induced Marangoni flow tends to dynamically suppress such a temperature gradient.

So far, regarding the possible influence of heat release on the droplet mixing, the analyses discussed previously have proposed three hypotheses: (a) heat release is insignificant during Mixing-Stage-1; (b) heat release from Zone 2 may transfer to the droplet surface during Mixing-Stage-2, inducing a temperature gradient from the bottom towards the top; (c) such a temperature gradient is assumed to be not large. To verify these hypotheses, we further refer to the experimental observations of Zhang *et al.* [27] for comparison. As shown in Fig. 13(b), during the initial stage of droplet impact ($t^* < 0.9$), no vapor is seen in the surrounding gas, thereby confirming hypothesis (a).

At $t^* = 0.9$, opaque vapors are seen at the bottom of the merged droplet, indicating evaporation starts first at this side, thereby justifying hypothesis (b). At $t^* = 2.1$ and $t^* = 3.6$, the droplet is surrounded by opaque vapors, indicating the entire droplet surface has been well heated up and, therefore, hypothesis (c) is substantiated.

Last but not least, even if the surface temperature gradient induces a thermal Marangoni effect during a later stage of the ignition delay and the interfacial Marangoni flow velocity reverses from the bottom back to the top, the aforementioned interpretation of experimental results is indeed not affected. Specifically, the nonmonotonic variation of internal mixing is caused by the competition between impact-inertia-driven-mixing and Marangoni-driven mixing, with the former enhanced and the latter suppressed by the impact inertia. As seen in Fig. 9, the first decrease of mixing index with impact inertia is ascribed to the wrap up process and therefore not affected by heat release; the second decrease, caused by the impact-inertia-driven interface stretch rate dl_i/dt , counteracts the Marangoni flow velocity u_{MF} . Physically, dl_i/dt is the velocity of the inertial frame of reference, while u_{Ma} is the velocity with respect to the frame regardless of the exact direction. Therefore, although the thermal Marangoni flow during the later stage of ignition delay may alter the internal flow and mixing structure, the negative effect of impact inertia on the Marangoni mixing is still present, and the aforementioned interpretation can still hold.

2. Monotonic decrease of IDT with impact inertia for ethanolamine solution of $\text{NaBH}_4/\text{H}_2\text{O}_2$ bipropellant

Finally, we consider the stoichiometric condition of ethanolamine solution of $\text{NaBH}_4/\text{H}_2\text{O}_2$. In this situation, the ethanolamine solution of NaBH_4 fuel droplet has a larger size and a lower surface tension and the H_2O_2

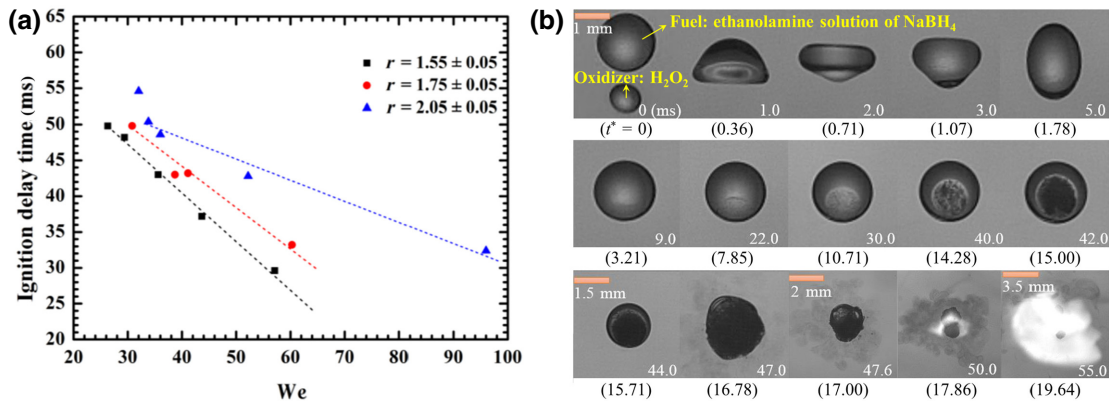


FIG. 14. (a) Monotonic variation of the IDT on the impact inertia (represented by the Weber number) for the ethanolamine solution of $\text{NaBH}_4/\text{H}_2\text{O}_2$ bipropellants. r is the size ratio of the WFNA droplet to the TMEDA droplet. (b) Shadowgraph images of the hypergolic ignition process at $We = 31$ and $\Delta = 1.75$. Adapted from Zhang [29].

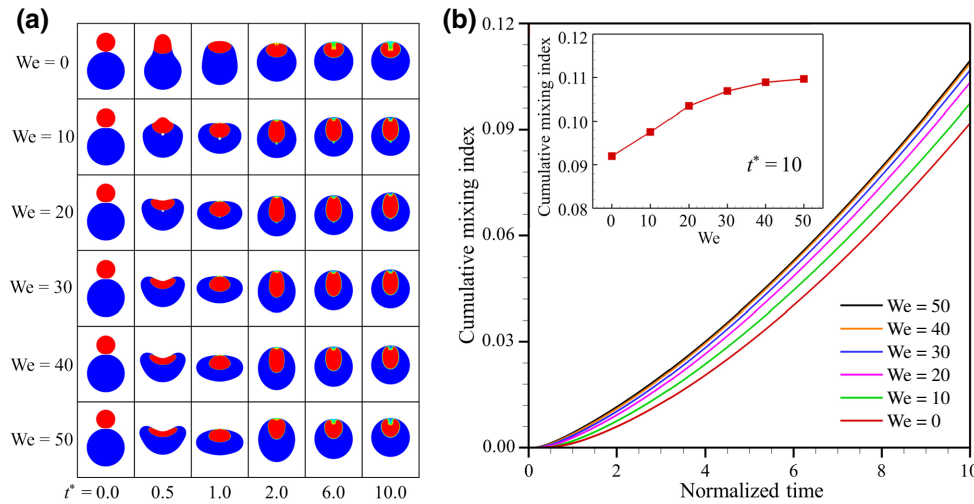


FIG. 15. (a) Collision and mixing of droplets at different We and fixed $\sigma^* = 0.5$ and $Oh = 0.1$. (b) Comparison of the temporal evolution of the cumulative mixing index of these cases, with the embedded inset comparing the values at $t^* = 10$.

oxidizer droplet has a smaller size and a higher surface tension; this fundamentally corresponds to the aforementioned scenario of $\sigma^* < 1$. In the experiment of Zhang [29], shown in Fig. 14(a), the IDT shows a monotonic decrease with increasing impact inertia, which could possibly correspond to a monotonic increase of internal mixing and is therefore inconsistent with the previously identified nonmonotonic increase-decrease-increase of the mixing index in the present study.

Such inconsistency could be due to the large viscous dissipation, since the viscosity of ethanolamine, the solvent of NaBH_4 , is 24.1 mPa s, which is over one order of magnitude larger than the viscosity of H_2O_2 . This can be substantiated by the slight degree of droplet deformation in Fig. 14(b). Therefore, we repeat the simulation of the cases in Figs. 9 and 10 with a significantly larger Ohnesorge number of 0.1. As shown in Fig. 15(a), the internal flow motion is substantially suppressed by the high viscous dissipation. Once the smaller droplet is wrapped up by the larger droplet, it cannot be further transported deep into the merged droplet and no vortical mixing structure can be formed. As a result, the Marangoni-driven mixing is substantially suppressed and the impact-inertia-driven fluid motion dominates the mixing process, which finally results in a monotonic increase of the mixing index with increasing Weber number [see Fig. 15(b)].

IV. CONCLUDING REMARKS

In the present paper, the internal mixing of head-on colliding droplets of different surface tensions is numerically studied to understand the fluidic mixing of bipropellants during hypergolic ignition. Simulations are performed at various Weber numbers and a fixed droplet size ratio of $\Delta = 2$. Two scenarios of surface tension difference are considered: (a) a lower-surface-tension smaller droplet colliding with a higher-surface-tension larger droplet, i.e., $\sigma^* > 1$, which corresponds to the stoichiometric condition

of a TMEDA/WFNA bipropellant system and is physically similar to a lower-surface-tension fuel/oxidizer droplet dripping onto a higher-surface-tension oxidizer/fuel pool; (b) a higher-surface-tension smaller droplet colliding with a lower-surface-tension larger droplet, i.e., $\sigma^* < 1$, which corresponds to the stoichiometric condition of an ethanolamine solution of $\text{NaBH}_4/\text{H}_2\text{O}_2$ bipropellant system and is physically similar to a higher-surface-tension fuel/oxidizer droplet dripping onto a lower-surface-tension oxidizer/fuel pool. A mixing index and a cumulative mixing index are used to quantify the degree of internal mixing. The simulations show that the Marangoni effect substantially enhances internal mixing, with $\sigma^* > 1$ being even more efficient compared with $\sigma^* < 1$.

For $\sigma^* > 1$, the internal mixing presents a nonmonotonic variation of decrease-increase-decrease-increase with the increase in We . The overall increase trend is caused by the mixing enhancement from the impact-inertia-driven spreading motion. The first decrease at a small We is due to a slight spreading motion that reduces the contact-surface-area:smaller-droplet-volume ratio during the wrap up process and thereby suppresses Marangoni-driven mixing. The second decrease at a large We is due to the increasing stretch of the deformed interface largely counteracting the Marangoni flow, which results in a reduced displacement velocity of the lower-surface-tension liquid on the interface and therefore weakens Marangoni-driven mixing.

For $\sigma^* < 1$, the internal mixing presents a simpler nonmonotonic variation of increase-decrease-increase with increasing We , which fundamentally corresponds to the latter part of the nonmonotonic variation of decrease-increase-decrease-increase for $\sigma^* > 1$. The absence of the increase at a small We is because the smaller droplet penetrates into the larger droplet shortly after coalescence, and the internal mixing largely relies on the long-time, post-wrap-up internal circulating flow rather than the short-time Marangoni-driven mixing during the wrap up process.

The results suggest that the nonmonotonic variation of the IDT with impact inertia for colliding hypergolic propellant droplets recently reported by Zhang *et al.* [27] is caused by the Marangoni-driven mixing rather than the capillary-driven jetlike mixing. Specifically, the TMEDA/WFNA bipropellant system is characterized by $\sigma^* > 1$, and the decrease-increase-decrease of IDT with increasing We could be ascribed to the aforementioned increase-decrease-increase of the mixing index with increasing We for $\sigma^* > 1$. For the ethanolamine solution of $\text{NaBH}_4/\text{H}_2\text{O}_2$ bipropellant system with $\sigma^* < 1$, the IDT decreases monotonically with increasing We, which is, however, inconsistent with the previously identified increase-decrease-increase of the mixing index with increasing We for $\sigma^* < 1$. This discrepancy, as verified by our further simulations, is because the large viscous dissipation substantially suppresses Marangoni-driven mixing, and the impact-inertia-driven spreading dominates the internal mixing.

Finally, the present results highlight the Marangoni effect in bipropellant droplet mixing, which could be a pivotal physical mechanism in hypergolic ignition. Despite binary droplet collision being employed as the specific object of study, the present results could also provide insight into the understanding of the hypergolic ignition of bipropellants using various mixing methodologies, such as impinging jet and droplet-pool impact. The present study has several implications: firstly, a shorter IDT of hypergolic bipropellants may not necessarily be caused by faster liquid-phase reactions, but could also be due to enhanced Marangoni mixing if their surface tension difference is large; secondly, further experimental measurements of the IDT of hypergolic propellants should provide a well-defined and precisely controlled condition for the fluidic mixing of the two liquids; thirdly, for the fuel injection system of hypergolic propellant engines, the collision between smaller-size, lower-surface-tension droplets and larger-size, higher-surface-tension droplets is preferred to facilitate bipropellant mixing and improve the ignition stability of the engines.

ACKNOWLEDGMENTS

This work is financially supported by the National Natural Science Foundation of China (No. 52076147) and the Tianjin Youth Talent Promotion Project (TJSQNTJ-2018-07). The work in the Hong Kong Polytechnic University is partially supported by DGRF (G-UAHP).

-
- [1] C. K. Law, Fuel options for next generation chemical propulsion, *AIAA J.* **50**, 19 (2012).
 - [2] E. Fletcher and G. Morrell, in *Progress in Combustion Science and Technology*, edited by J. Ducarme, M. Gerstein, A. H. Lefebvre (Elsevier, Pergamon, 1960), pp. 183–215.

- [3] C. McKinney and M. Kilpatrick, An apparatus for measuring the rates of some rapid reactions, *Rev. Sci. Instrum.* **22**, 590 (1951).
- [4] M. Kilpatrick and L. Baker, A study of fast reactions in fuel-oxidant systems: Anhydrous hydrazine with 100 percent nitric acid, *Symp. (Int.) Combust.* **5**, 196 (1955).
- [5] R. Schalla and E. Pletcher, The behavior of the system triethylamine-white fuming nitric acid under conditions of rapid mixing, *Symp. (Int.) Combust.* **6**, 911 (1957).
- [6] R. Schalla, The ignition behavior of various amines with white fuming nitric acid, *ARS J.* **29**, 33 (1959).
- [7] J. Dennis, T. Pourpoint, and S. Son, in the 47th AIAA/ASME/SAE/ASEE Joint Propulsion Conference & Exhibit, American Institute of Aeronautics and Astronautics (AIAA, San Diego, California, 2011).
- [8] J. Dennis, S. Son, and T. Pourpoint, in the 48th AIAA/ASME/SAE/ASEE Joint Propulsion Conference & Exhibit, American Institute of Aeronautics and Astronautics (AIAA, Atlanta, Georgia, 2012).
- [9] D. Bittner, J. Sell, and G. Risha, in the 49th AIAA/ASME/SAE/ASEE Joint Propulsion Conference & Exhibit, American Institute of Aeronautics and Astronautics (AIAA, San Jose, CA, 2013).
- [10] H. Tani, Y. Daimon, M. Sasaki, and Y. Matsuura, Atomization and hypergolic reactions of impinging streams of monomethylhydrazine and dinitrogen tetroxide, *Combust. Flame* **185**, 142 (2017).
- [11] T. Pourpoint and W. Anderson, in the 41th AIAA/ASME/SAE/ASEE Joint Propulsion Conference & Exhibit, American Institute of Aeronautics and Astronautics (AIAA, Tucson, Arizona, 2005).
- [12] B. Jyoti, M. Naseem, S. Baek, H. Lee, and S. Cho, Hypergolicity and ignition delay study of gelled ethanolamine fuel, *Combust. Flame* **183**, 102 (2017).
- [13] H. Kang, S. Park, Y. Park, and J. Lee, Ignition-delay measurement for drop test with hypergolic propellants: Reactive fuels and hydrogen peroxide, *Combust. Flame* **217**, 306 (2020).
- [14] X. Weng, C. Tang, J. Li, Q. Zhang, and Z. Huang, Coulomb explosion and ultra-fast hypergolic ignition of borohydride-rich ionic liquids with WFNA, *Combust. Flame* **194**, 464 (2018).
- [15] V. Bhosale, J. Jeong, J. Choi, D. Churchill, Y. Lee, and S. Kwon, Additive-promoted hypergolic ignition of ionic liquid with hydrogen peroxide, *Combust. Flame* **214**, 426 (2020).
- [16] V. Bhosale, S. Karnik, and P. Kulkarni, Ignition study of amine borane/cyanoborane based green hypergolic fuels, *Combust. Flame* **210**, 1 (2019).
- [17] C. Sun, S. Tang, and X. Zhang, Hypergolicity evaluation and prediction of ionic liquids based on hypergolic reactive groups, *Combust. Flame* **205**, 441 (2019).
- [18] S. Wang and S. Thynell, An experimental study on the hypergolic interaction between monomethylhydrazine and nitric acid, *Combust. Flame* **159**, 438 (2012).
- [19] E. Dambach, K. Cho, T. Pourpoint, and S. Heister, in the 46th AIAA/ASME/SAE/ASEE Joint Propulsion Conference & Exhibit, American Institute of Aeronautics and Astronautics (AIAA, Nashville, TN, 2010).
- [20] W. Florczuk and G. Rarata, in the 66th International Astronautical Federation Congress, International

- Astronautical Federation (International Astronautical Federation, Jerusalem, Israel, 2015).
- [21] B. Jyoti, M. Naseem, and S. Baek, Hypergolicity and ignition delay study of pure and energized ethanol gel fuel with hydrogen peroxide, *Combust. Flame* **176**, 318 (2017).
 - [22] S. Davis and N. Yilmaz, Advances in hypergolic propellants: Ignition, hydrazine, and hydrogen peroxide research, *Adv. Aerosp. Eng.* **2014**, 1 (2014).
 - [23] J. Forness, T. Pourpoint, and S. Heister, in the 49th AIAA/ASME/SAE/ASEE Joint Propulsion Conference & Exhibit, American Institute of Aeronautics and Astronautics (AIAA, San Jose, CA, 2013).
 - [24] J. John, P. Nandagopalan, S. Baek, and S. Cho, Hypergolic ignition delay studies of solidified ethanol fuel with hydrogen peroxide for hybrid rockets, *Combust. Flame* **212**, 205 (2020).
 - [25] E. Dambach, Y. Solomon, S. Heister, and T. Pourpoint, Investigation into the hypergolic ignition process initiated by low Weber number collisions, *J. Propul. Power* **29**, 331 (2013).
 - [26] B. Natan, V. Perteghella, and Y. Solomon, Hypergolic ignition by fuel gellation and suspension of reactive or catalyst particles, *J. Propul. Power* **27**, 1145 (2011).
 - [27] D. Zhang, P. Zhang, Y. Yuan, and T. Zhang, Hypergolic ignition by head-on collision of N,N,N',N'-tetramethylethylenediamine and white fuming nitric acid droplets, *Combust. Flame* **173**, 276 (2016).
 - [28] D. Zhang, C. He, P. Zhang, and C. Tang, Mass interminglement and hypergolic ignition of TMEDA and WFNA droplets by off-center collision, *Combust. Flame* **197**, 267 (2018).
 - [29] D. Zhang, Ph.D. thesis, The Hong Kong Polytechnic University, 2018.
 - [30] D. Zhang, D. Yu, P. Zhang, Y. Yuan, L. Yue, T. Zhang, and X. Fan, Hypergolic ignition modulated by head-on collision, intermixing and convective cooling of binary droplets with varying sizes, *Int. J. Heat Mass Transf.* **139**, 475 (2019).
 - [31] C. Tang, J. Zhao, P. Zhang, and C. K. Law, Dynamics of internal jets in the merging of two droplets of unequal sizes, *J. Fluid Mech.* **795**, 671 (2016).
 - [32] K. Sun, P. Zhang, C. K. Law, and T. Wang, Collision Dynamics and Internal Mixing of Droplets of Non-Newtonian Liquids, *Phys. Rev. Appl.* **4**, 054013 (2015).
 - [33] K. Sun, T. Wang, P. Zhang, and C. K. Law, Non-Newtonian flow effects on the coalescence and mixing of initially stationary droplets of shear-thinning fluids, *Phys. Rev. E* **91**, 023009 (2015).
 - [34] K. Sun, P. Zhang, M. Jia, and T. Wang, Collision-induced jet-like mixing for droplets of unequal-sizes, *Int. J. Heat Mass Transf.* **120**, 218 (2018).
 - [35] X. Chen and V. Yang, Direct numerical simulation of multiscale flow physics of binary droplet collision, *Phys. Fluids* **32**, 062103 (2020).
 - [36] D. Lohse and X. Zhang, Physicochemical hydrodynamics of droplets out of equilibrium, *Nat. Rev. Phys.* **2**, 426 (2020).
 - [37] R. Koldewij, B. van Capelleveen, D. Lohse, and C. Visser, Marangoni-driven spreading of miscible liquids in the binary pendant drop geometry, *Soft Matter* **15**, 8525 (2019).
 - [38] F. Blanchette, Simulation of Mixing Within Drops due to Surface Tension Variations, *Phys. Rev. Lett.* **105**, 074501 (2010).
 - [39] F. Jia, K. Sun, P. Zhang, C. Yin, and T. Wang, Marangoni effect on the impact of droplets onto a liquid-gas interface, *Phys. Rev. Fluids* **5**, 073605 (2020).
 - [40] C. Visser, T. Kamperman, L. Karbaat, D. Lohse, and M. Karperien, In-air microfluidics enables rapid fabrication of emulsions, suspensions, and 3D modular (bio) materials, *Sci. Adv.* **4**, 1175 (2018).
 - [41] D. Jacqmin, Calculation of two-phase Navier-Stokes flows using phase-field modeling, *J. Comput. Phys.* **155**, 96 (1999).
 - [42] P. Yue, J. Feng, C. Liu, and J. Shen, A diffuse-interface method for simulating two-phase flows of complex fluids, *J. Fluid Mech.* **515**, 293 (2004).
 - [43] T. Lee, Effects of incompressibility on the elimination of parasitic currents in the lattice Boltzmann equation method for binary fluids, *Comput. Math. Appl.* **58**, 987 (2009).
 - [44] T. Lee and L. Liu, Lattice Boltzmann simulations of microscale drop impact on dry surfaces, *J. Comput. Phys.* **229**, 8045 (2010).
 - [45] K. Sun, P. Zhang, Z. Che, and T. Wang, Marangoni-flow-induced partial coalescence of a droplet on a liquid/air interface, *Phys. Rev. Fluids* **3**, 023602 (2018).
 - [46] Q. Li, K. Luo, and Q. Kang, Lattice Boltzmann methods for multiphase flow and phase-change heat transfer, *Prog. Energ. Combust. Sci.* **52**, 62 (2016).
 - [47] Q. Li, K. Luo, and X. Li, Lattice Boltzmann modeling of multiphase flows at large density ratio with an improved pseudopotential model, *Phys. Rev. E* **87**, 053301 (2013).
 - [48] Q. Li and K. Luo, Achieving tunable surface tension in the pseudopotential lattice Boltzmann modeling of multiphase flows, *Phys. Rev. E* **88**, 053307 (2013).
 - [49] D. Lycett-Brown and K. Luo, Cascaded lattice Boltzmann method with improved forcing scheme for large-density-ratio multiphase flow at high Reynolds and Weber numbers, *Phys. Rev. E* **94**, 053313 (2016).
 - [50] K. Sun, M. Jia, and T. Wang, Numerical investigation on the head-on collision between unequal-sized droplets with multiple-relaxation-time lattice Boltzmann model, *Int. J. Heat Mass Transf.* **70**, 629 (2014).
 - [51] S. Gottlieb and C. Shu, Total variation diminishing Runge-Kutta schemes, *Math. Comp.* **67**, 73 (1998).
 - [52] G. Jiang and C. Shu, Efficient implementation of weighted ENO schemes, *J. Comput. Phys.* **126**, 202 (1996).
 - [53] K. Pan, P. Chou, and Y. Tseng, Binary droplet collision at high Weber number, *Phys. Rev. E* **80**, 036301 (2009).
 - [54] C. Kuan, K. Pan, and W. Shyy, Study on high-Weber-number droplet collision by a parallel, adaptive interface-tracking method, *J. Fluid Mech.* **759**, 104 (2014).
 - [55] M. Liu and D. Bothe, Numerical study of head-on droplet collisions at high Weber numbers, *J. Fluid Mech.* **789**, 785 (2016).
 - [56] See Supplemental Material at <http://link.aps.org/supplemental/10.1103/PhysRevApplied.15.034076> for temporal evolution of the spreading distance of the lower-surface-tension-fluid, grid dependence study, and comparison of the mixing index and the cumulative mixing index at low Weber numbers.